

Geodetically Accurate InSAR Data Processor

Howard A. Zebker, *Fellow, IEEE*, Scott Hensley, Piyush Shanker, and Cody Wortham

Abstract—We present a new interferometric synthetic aperture radar (InSAR) processing approach that capitalizes on the precise orbit tracking that is available with modern radar satellites. Our method uses an accurate orbit information along with motion-compensation techniques to propagate the radar echoes to positions along a noninertial virtual orbit frame in which the location and focusing equations are particularly simple, so that images are focused without requiring autofocus techniques and are computed efficiently. Motion compensation requires two additional focus correction phase terms that are implemented in the frequency domain. If the images from an interferometric pair or stack are all computed along the same reference orbit, flat-Earth topographic correction is not needed, and image coregistration is simplified, obviating many difficulties that are often encountered in InSAR processing. We process several data sets collected by the ALOS PALSAR instrument and find that the geodetic accuracy of the radar images is 10–20 m, with up to 20 m of additional image distortion needed to align $100 \text{ km} \times 100 \text{ km}$ scenes with reference digital elevation models. We validated the accuracy by using both known radar corner reflector locations and by the registration of the interferograms with digital maps. The topography-corrected interferograms are free from all geometric phase terms, and they clearly show the geophysical observables of crustal deformation, atmospheric phase, and ionospheric phase.

Index Terms—Interferometric synthetic aperture radar (InSAR), motion compensation, radar interferometry, SAR processing, synthetic aperture radar (SAR).

I. INTRODUCTION

INTERFEROMETRIC synthetic aperture radar (InSAR) has evolved into a common tool for analysis of crustal deformation [1]–[8], ice motion and structure [9]–[14], hydrologic modeling [15]–[17], vegetation canopy characterization [18]–[20], and generation of topographic data [21]–[24]. The InSAR technique is defined by computing the phase difference of complex radar echoes at each resolution element in a radar image, resulting in millimeter-scale displacement images at meter-level postings over wide areas (typically 100-km scales). Recent developments in satellite tracking and radar signal processing now permit the generation of InSAR images or interferograms that are, in addition, geodetically quite accurate. The geodetic accuracy not only provides data products in better known coordinate systems but also facilitates routine processing by avoiding many of the image registration and

resampling steps incorporated into existing processing systems. The algorithms presented here are computationally efficient and more robust than many traditional processing approaches, enabling advanced approaches to data interpretation such as time series analysis of surface change.

The continuing advances in the accuracy of orbit determination now routinely produce spacecraft position estimates with submeter uncertainties. Satellites such as the European ERS-1 and ERS-2, Envisat, and Japanese ALOS produce operational products with standard errors of tens of centimeters or less [25]–[28]. We have designed a new software radar processing system based on these accurate orbit measurements so that the radar pixels may be located on the surface with accuracies of tens of meters or less. In our approach, we use radar motion-compensation techniques to propagate radar echoes from their actual acquisition locations to ideal orbits in which the focusing and positioning equations are particularly simple. Thus, when processing multiple images, for a case that is as simple as two scenes to be formed into a single interferogram or as complex as hundreds of scenes to form a persistent scattering estimate of temporal evolution of crustal deformation, all of the data passes may be processed to a common coordinate system. This facilitates the resampling of the individual single-look complex scenes to common locations, which is a step that is often problematic in geodetically inaccurate processing methods. The accuracy of the orbits is such that autofocus or other image refinement steps are not necessary, significantly increasing both the efficiency of the processor and the accuracy to which pixels may be located on the surface. Another advantage to motion-compensated processing using a common reference orbit is that the “curved-Earth” range phase term is not present in the interferograms as the effective InSAR baseline, as regards Earth curvature, is zero.

Here, we describe our processing method, starting with the definition of our reference orbit and the equations needed for radar image focusing and pixel location. We then summarize our motion-compensation approach and show that two focus correction phase histories must be added to the radar echo to properly focus the image. We then describe an iterative algorithm for mapping the interferograms, as expressed in radar coordinates, to evenly spaced and known geodetic coordinates so that the images may be readily combined with other data types. We assess the geodetic accuracy of the system by analyzing the data acquired over a set of GPS-surveyed radar corner reflectors. Finally, we present several interferograms from L-band ALOS PALSAR data in order to demonstrate applicability to a variety of applications.

We note that our method is not necessarily more geodetically accurate than other InSAR software that has been similarly motivated. We have attempted to design a processing system

Manuscript received October 23, 2009; revised March 18, 2010. Date of publication July 15, 2010; date of current version November 24, 2010.

H. A. Zebker, P. Shanker, and C. Wortham are with the Departments of Electrical Engineering and Geophysics, Stanford University, Stanford, CA 94305-2155 USA (e-mail: zebker@stanford.edu).

S. Hensley is with the Jet Propulsion Laboratory, California Institute of Technology, Pasadena, CA 91109 USA.

Color versions of one or more of the figures in this paper are available online at <http://ieeexplore.ieee.org>.

Digital Object Identifier 10.1109/TGRS.2010.2051333

with geodetic accuracy as a fundamental design consideration. Hence, a major emphasis in this paper is on useful coordinate systems to facilitate geodetic accuracy in both the SAR processing and the derivation of InSAR products. Geodetic accuracy is not only important for many applications but also readily feasible in today's precise-orbit world, as we demonstrate in the succeeding discussion.

Previous presentations of geodetically accurate radar processing [29], [30] also show accuracies that are roughly the size of a 10-m radar resolution cell. The work at Scripps Institution of Oceanography [30] has already shown that orbit accuracy for the ALOS satellite is fine enough to obviate the need for autofocus modules in the software. We find similarly that this code is unneeded. In addition, several groups [31]–[34] have experimented with aligning time sequences of images precisely during processing to a single master image. In our approach, we do the same, but the coordinate system used is not a physically realizable system for a satellite in an inertial orbit. In essence, we use a virtual coordinate system to simplify postprocessing codes that implement the InSAR product generation.

It is worth noting that the motion-compensation approach that we present here is a critical aspect for processing SAR data from airborne platforms, where interactions with the atmosphere lead to turbulent flight trajectories that defocus SAR images and lead to InSAR phase errors. These short-period orbit errors are usually less significant for spaceborne platforms that generally orbit well above the atmosphere, although they can be present for certain system configurations or imaging geometries. In this paper, we meet precise geometrical standards using an approach that can work even with very irregular orbits, such as those that might arise from low-altitude satellites or from platforms with extremely long synthetic apertures, as required for long-wavelength radar systems.

II. PHASE HISTORY FOR SPACECRAFT IN PERFECT CIRCULAR ORBIT

We begin by developing the equations needed to properly locate and focus a SAR image from an orbiting radar sensor. Assume that we have a satellite in a perfect circular orbit above a nonrotating planet. Since all known planets rotate, such an orbital is noninertial, it cannot exist in a physical sense without continuous accelerations applied to the spacecraft, and, thus, it is not feasible for satellites in use today. Nonetheless, we can define such an orbit and translate the actual radar echoes to the ideal reference trajectory using motion-compensation methods. We define the geometry of the spacecraft radar observing a point P as shown in Fig. 1.

Here, the spacecraft travels along an orbit path at a constant velocity v , at a constant height h , and above a spherical planet with a radius of curvature r_c . The range to the imaged point r varies as a function of time t . The usual relations for radar phase history ϕ and instantaneous frequency f hold

$$\phi(t) = -\frac{4\pi}{\lambda} r(t) \quad (1)$$

$$2\pi f(t) = -\frac{4\pi}{\lambda} \dot{r}(t). \quad (2)$$

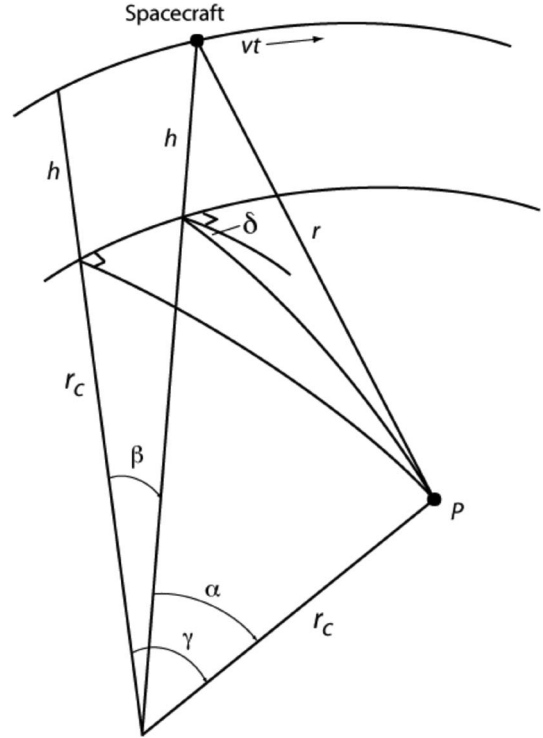


Fig. 1. Definitions of angles and distances for the reference orbit. The planet is assumed to be locally spherical with a radius of curvature r_c , and note that r_c is not necessarily equal to the local distance from the surface to the center of mass of the Earth. The spacecraft flies at an altitude h above the surface and on a perfect circular path about a point r_c below the surface. The point P that is to be imaged lies at an origin-centered angle γ from the satellite orbit at the closest approach. The distance along the orbit is equal to the spacecraft velocity v multiplied by time t , so that at any given time, the satellite-origin-closest approach point angle is β . The origin-centered angle α is formed by the point to be imaged, the origin, and the satellite location. Angle δ is the squint angle from the satellite to the imaged point.

The Doppler frequency f_D and the Doppler rate f_{rate} , respectively, can be written as

$$f_D = -\frac{2}{\lambda} \dot{r} \quad (3)$$

$$f_{rate} = -\frac{2}{\lambda} \ddot{r}. \quad (4)$$

We now relate these general expressions to the geometry of Fig. 1. From the law of cosines

$$r^2 = (h + r_c)^2 + r_c^2 - 2r_c(h + r_c) \cos \alpha. \quad (5)$$

The spherical law of cosines considering the right angle shown in the figure is equal to

$$\cos \alpha = \cos \beta \cos \gamma. \quad (6)$$

Let us rewrite this as

$$r^2 = (h + r_c)^2 + r_c^2 - 2r_c(h + r_c) \cos \beta \cos \gamma. \quad (7)$$

By noting that $vt/(h + r_c) = \beta$, and $\dot{\beta} = v/(h + r_c)$ is a constant, we can differentiate (7) with respect to time

$$2r\dot{r} = -2r_c(h + r_c) \cos \gamma (-\sin \beta) \dot{\beta}. \quad (8)$$

Thus

$$\dot{r} = \frac{r_c(h + r_c) \cos \gamma \sin \beta \dot{\beta}}{r} \quad (9)$$

or it is expressed as f_D as a function of the along-track angle β

$$f_D = -\frac{2}{r\lambda} r_c(h + r_c) \cos \gamma \sin \beta \dot{\beta}. \quad (10)$$

To determine the SAR focusing parameter f_{rate} , we start with (8) and again differentiate with respect to time, obtaining

$$\begin{aligned} r\ddot{r} + \dot{r}^2 &= r_c(h + r_c) \cos \gamma \dot{\beta} \cos \beta \dot{\beta} \\ &= r_c(h + r_c) \cos \gamma \sin \beta \dot{\beta} \cdot \frac{\cos \beta}{\sin \beta} \dot{\beta} \\ &= r\dot{r} \frac{\cos \beta}{\sin \beta} \dot{\beta}. \end{aligned} \quad (11)$$

Then

$$r\ddot{r} = r\dot{r} \frac{\cos \beta}{\sin \beta} \dot{\beta} - \dot{r}^2 \quad (12)$$

$$\ddot{r} = \dot{r} \frac{\cos \beta}{\sin \beta} \dot{\beta} - \frac{\dot{r}^2}{r} \quad (13)$$

finally yielding

$$f_{\text{rate}} = \frac{2}{\lambda} \left[\frac{\dot{r}^2}{r} - \dot{r} \frac{\cos \beta}{\sin \beta} \dot{\beta} \right]. \quad (14)$$

The expressions for f_D and f_{rate} , which are (10) and (14), respectively, supply the information that is necessary for locating the along-track position and the optimal chirp rate to image point P , as in many range Doppler processing implementations (see, for example, [35]).

III. MOTION-COMPENSATION APPROACH AND GEOMETRY

Thus, if the spacecraft was flying in the above ideal orbit, we can readily construct the matched filter for an along-track location, as given by the Doppler centroid f_D and azimuth chirp rate f_{rate} . However, it would be very wasteful of fuel to force a satellite into this noninertial orbit, and existing sensors do not follow such an orbital trajectory. We therefore apply a motion-compensation algorithm to the received echoes so that the data are similar to what the sensor would have recorded if it had flown along the reference track. In addition to allowing ready focusing and identifying the location of the image using the equations of the previous section, the motion-compensation step allows us to process multiple acquisitions to the same coordinate system.

We introduce here a coordinate system that is defined with respect to the projected ground track of the ideal satellite orbit. This coordinate system, referred to as sch , was developed and used for the NASA Shuttle Radar Topography Mission at the Jet Propulsion Laboratory [36]. In this coordinate system, s is the along-track coordinate along the surface projection of the satellite path, c is the cross-track coordinate along the surface

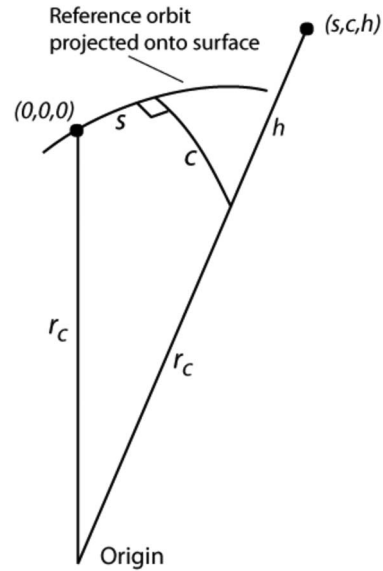


Fig. 2. Definition of the sch coordinate system. A reference point along the reference orbit has coordinates $(0,0,0)$, and the local Earth radius of curvature is r_c . An arbitrary point in space (s, c, h) is located at a height h above the spherical surface and at a surface distance c from the projection of the reference point and is displaced along track by s . The reference orbit is assumed to be perfectly circular and centered about the origin shown.

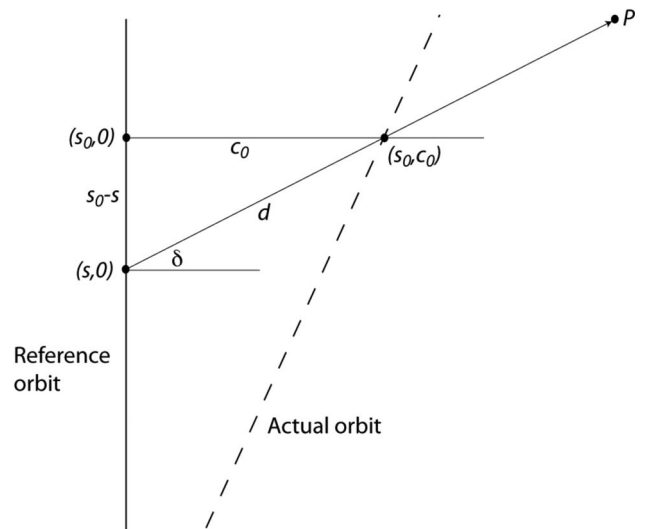


Fig. 3. Motion-compensation geometry and position definitions. The projection of the actual satellite orbit on the planet surface is the dashed line, and the desired reference orbit projects as the solid line. The spacecraft observes a point P when it is located above (s_0, c_0) . The squint angle δ is defined by the Doppler centroid. The virtual position of the spacecraft after motion compensation is at point $(s, 0)$, and distance d is the surface projection of the amount where the echo must be propagated to represent what the sensor would have measured if it had indeed been located at $(s, 0)$.

to the projection of a point, and h is the height of the point above the surface (Fig. 2).

Consider a top-down view of the motion-compensation reference orbit and the actual ground track of the satellite projected on a spherical planet, as shown in Fig. 3.

Here, the actual location of the satellite is (s_0, c_0, h_0) ; P is the point to be imaged; δ is the squint angle, given the Doppler centroid of the point; the desired position of the motion-compensated satellite is $(s, 0, h)$; and c_0 , $s - s_0$, and

d are all distances along great circles on the planet surface. Once again, starting with the spherical law of cosines, we see

$$\cos \frac{d}{r_c} = \cos \frac{s_0 - s}{r_c} \cos \frac{c_0}{r_c} \quad (15)$$

while the law of sines yields

$$\frac{\sin(\pi/2 - \delta)}{\sin \frac{c_0}{r_c}} = \frac{\sin \pi/2}{\sin \frac{d}{r_c}}. \quad (16)$$

In addition, we can also write using the spherical law of cosines

$$\cos(\pi/2 - \delta) \sin \frac{s_0 - s}{r_c} \sin \frac{d}{r_c} + \cos \frac{s_0 - s}{r_c} \cos \frac{d}{r_c} = \cos \frac{c_0}{r_c}. \quad (17)$$

By using (15) earlier

$$\cos(\pi/2 - \delta) \sin \frac{s_0 - s}{r_c} \sin \frac{d}{r_c} + \cos^2 \frac{s_0 - s}{r_c} \cos \frac{c_0}{r_c} = \cos \frac{c_0}{r_c} \quad (18)$$

or

$$\begin{aligned} \cos(\pi/2 - \delta) \sin \frac{s_0 - s}{r_c} \sin \frac{d}{r_c} &= \cos \frac{c_0}{r_c} \left(1 - \cos^2 \frac{s_0 - s}{r_c}\right) \\ &= \cos \frac{c_0}{r_c} \sin^2 \frac{s_0 - s}{r_c} \end{aligned} \quad (19)$$

and thus

$$\cos(\pi/2 - \delta) \sin \frac{d}{r_c} = \cos \frac{c_0}{r_c} \sin \frac{s_0 - s}{r_c}. \quad (20)$$

Moreover, from (16)

$$\cos(\pi/2 - \delta) \frac{\sin \frac{c_0}{r_c}}{\sin(\pi/2 - \delta)} = \cos \frac{c_0}{r_c} \sin \frac{s_0 - s}{r_c} \quad (21)$$

from which

$$\tan \delta \sin \frac{c_0}{r_c} = \cos \frac{c_0}{r_c} \sin \frac{s_0 - s}{r_c}. \quad (22)$$

Finally

$$\tan \delta \tan \frac{c_0}{r_c} = \sin \frac{s_0 - s}{r_c}. \quad (23)$$

Now, we can solve for the desired spacecraft position s

$$s = s_0 - r_c \sin^{-1} \left(\tan \delta \tan \frac{c_0}{r_c} \right). \quad (24)$$

The desired cross-track position and height are 0 and h , respectively, so now, we know both the actual and motion-compensated spacecraft locations. The solution for the composite squint angle δ can be found from the aforementioned α , β , and γ since (again from the spherical law of cosines)

$$\sin \delta = \frac{(\cos \gamma - \cos \beta \cos \alpha)}{\sin \beta \sin \alpha}. \quad (25)$$

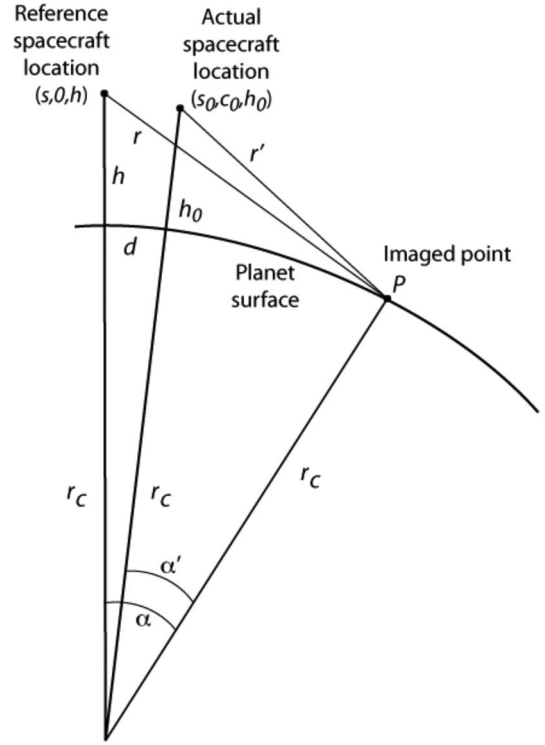


Fig. 4. Motion-compensation distances. The echo must be propagated from an actual distance r' to a desired distance r . The shift corresponds to a change in angle $\alpha - \alpha'$ that is relevant to the surface shift d in Fig. 3.

IV. MOTION-COMPENSATION ALGORITHM

The equations in the previous section provide the relationship between the actual spacecraft locations and the desired imaging locations along the reference orbit. The satellite is not flying in this ideal orbit, of course, so we propagate the radar echoes from the actual satellite position to the ideal reference track to make it appear as if the radar had flown the perfect circular path described earlier, which is a procedure known as motion compensation (a good description is found in [37]).

We use an approximate form for motion compensation by assuming that the appropriate displacement for a scatterer is the one that is associated with its location at the point where the scatterer passes through the antenna boresight. This approximation is most valid for systems with a narrow antenna beam. In other words, we assume that most of the backscattered energy comes from a direction that corresponds to the Doppler centroid of the echo. This approximation is quite good for many existing spaceborne radar systems, although it leads to a focusing error because echoes from the scatterer that are away from the boresight are slightly shifted in phase. This phase error is corrected in the azimuth focusing step, which we explain in the following focusing section.

We apply the motion-compensation resampling to the measured data by adding to the echo the appropriate phase and by shifting its position in time according to the motion-compensation distance. The distance where the echo must be shifted is readily seen in the following (Fig. 4).

For the motion-compensation algorithm, we use the actual distance from the spacecraft (s_0, c_0, h_0) to the point P (denoted as r') as measured by the radar and the calculated

distance (denoted as r in Figs. 1 and 4) from the motion-compensated reference track $(s, 0, h)$. We determine the origin-centered angles α and α' for the reference and actual positions starting with

$$\cos \alpha' = \frac{(r_c + h_0)^2 + r_c^2 - r'^2}{2r_c(h_0 + r_c)} \quad (26)$$

and by using the difference $\alpha - \alpha'$ (which is equal to d/r_c), we find that the cosine of the origin-centered angle α for the reference location is

$$\cos \alpha = \cos \alpha' \cos \frac{d}{r_c} - \sin \alpha' \sin \frac{d}{r_c} \quad (27)$$

so that

$$r = \sqrt{(r_c + h)^2 + r_c^2 - 2(r_c + h)r_c \cos \alpha}. \quad (28)$$

We then shift the position of the return echo by $r' - r$ and its phase by $(4\pi/\lambda)(r' - r)$. Since r' is a function of r , we can express the motion-compensation baseline and phase, respectively, as

$$b = r'(r) - r \quad (29)$$

$$\phi_{\text{baseline}} = \frac{4\pi}{\lambda} (r'(r) - r). \quad (30)$$

V. FOCUS CORRECTIONS

Two phase correction terms are needed to properly focus the motion-compensated SAR images. The first correction is a change in the Doppler frequency rate f_{rate} resulting from the motion-compensation shift in the scatterer distance from the radar. The second correction is a phase term added to the phase history to account for range dependence of the motion-compensation phase shift.

The echo signal after motion compensation is moved to a different range if the motion-compensation baseline (the difference between the actual spacecraft position and the position projected onto the reference orbit as described earlier) is nonzero. The phase history of a scatterer, which depends on actual imaging geometry, is thus located at a different range than its original position, and it differs from the history that is expected at its motion-compensated range. While motion compensation adequately corrects the constant and linear terms for the phase history, the second order term requires an additional correction. The first correction factor changes the frequency rate of the matched filter by the ratio of the motion-compensation baseline (the distance that the echo moved in the motion-compensation step) to the scatterer range. Consider the following (Fig. 5).

This figure shows a simplified motion-compensation geometry that is constrained so that the reference orbit, the actual orbit, and the scattering point are all coplanar, and we assume that we are processing the echo that is centered at the zero Doppler point. The distance $b(t)$ is the motion-compensation baseline. The range history for the scatterer with respect to the reference orbit satisfies

$$r^2(t) = r_0^2 + v^2 t^2 \quad (31)$$

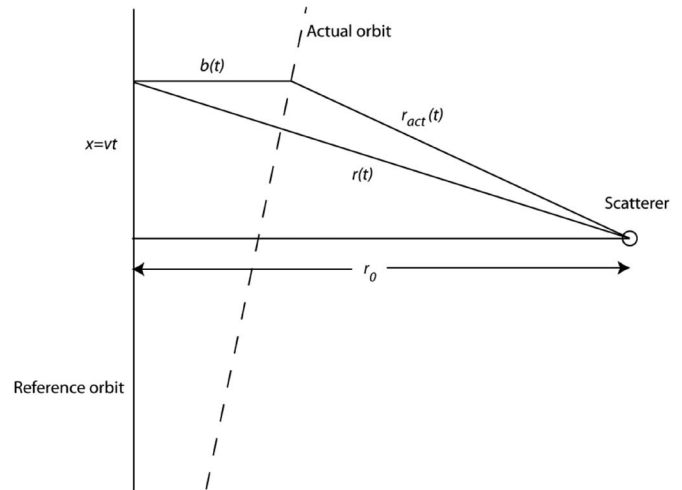


Fig. 5. Geometric construction to understand the Doppler rate correction required after motion compensation. In this simplified geometry, the reference orbit, the actual orbit, and the scatterer all lie in the plane of the page. The actual distance from the spacecraft to the scatterer is $r_{\text{act}}(t)$, and the distance of the motion-compensated spacecraft along the reference orbit to the scatterer is $r(t)$. The distance from the reference spacecraft to the scatterer at the closest approach is r_0 , and $b(t)$ is the motion-compensation baseline as a function of time.

which, under the usual SAR approximation, can be written as

$$r(t) \approx r_0 + \frac{1}{2} \frac{v^2 t^2}{r_0} \quad (32)$$

leading to a Doppler rate $f_{\text{rate}} = -(2v^2/\lambda r_0)$.

The range history of the actual return from the scatterer, again under the SAR approximation, is

$$\begin{aligned} r_{\text{act}}(t) &\approx r_0 - b(t) + \frac{1}{2} \frac{v^2 t^2}{(r_0 - b(t))} \\ &\approx r_0 - b(t) + \frac{1}{2} \frac{v^2 t^2}{r_0} \left(1 + \frac{b(t)}{r_0}\right). \end{aligned} \quad (33)$$

Next, note that, in the motion-compensation step, we add the value of the baseline to this to form the motion-compensated range history, resulting in

$$r_{\text{mocomp}}(t) = r_0 + \frac{1}{2} \frac{v^2 t^2}{r_0} \left(1 + \frac{b(t)}{r_0}\right). \quad (34)$$

Comparing with the reference range history earlier shows that the Doppler rate that is needed to focus the echo is the same as the reference rate, scaled by a factor that depends on the ratio of the motion-compensation baseline to the range. In other words, since the scatterer is moved to a different range than its original location, the focus must be corrected to account for this distortion. The correction factor does depend on the varying baseline with time, but in practice, we find that using a constant value for each processed patch of data is sufficiently precise for many radar satellites.

To calculate the change in f_{rate} for the full geometry rather than the simplified case of Fig. 5, note that we

can write

$$\begin{aligned}
 f_{\text{rate}} &= \frac{2}{\lambda} \left[\frac{\dot{r}^2}{r} - \dot{r} \frac{\cos \beta}{\sin \beta} \dot{\beta} \right] \\
 &= \frac{2}{\lambda} \left[\frac{\lambda^2 f_D^2}{4r} + \frac{\lambda}{2} \frac{f_D}{\tan \beta} \dot{\beta} \right] \\
 &= \frac{\lambda f_D^2}{2r} - \frac{2v^2}{\lambda r} \frac{r_c}{(h+r_c)} \cos \alpha. \quad (35)
 \end{aligned}$$

Thus, the difference in f_{rate} for the scatterer at its original position (primed coordinates) and its motion-compensated position is

$$\begin{aligned}
 f_{\text{rate}} - f'_{\text{rate}} &= \frac{\lambda f_D^2}{2} \left(\frac{1}{r} - \frac{1}{r'} \right) - \frac{2v^2}{\lambda} \frac{r_c}{(h+r_c)} \\
 &\quad \times \left(\frac{\cos \alpha}{r} - \frac{\cos \alpha'}{r'} \right) \\
 &= \frac{\lambda f_D^2}{2} \left(\frac{r' - r}{rr'} \right) - \frac{2v^2}{\lambda} \frac{r_c}{(h+r_c)} \\
 &\quad \times \left(\frac{r' \cos \alpha - r \cos \alpha'}{rr'} \right) \\
 &\approx \frac{\lambda f_D^2}{2r} \frac{b(t)}{r} - \frac{2v^2}{\lambda r} \frac{r_c}{(h+r_c)} \cos \alpha \frac{b(t)}{r} \\
 &= f_{\text{rate}} \frac{b(t)}{r} \quad (36)
 \end{aligned}$$

which is the same relation that we had in the simplified case for $r = r_0$ and which holds under the same approximation of slowly changing $b(t)$ for each patch and for $h \approx h'$.

A second focus correction factor is required as well to compensate for the phase added to each radar echo during motion compensation. Recall that each echo has been altered by a range-varying phase of the form given in (30). Due to range migration, this phase varies as a function of the range migration distance for each scatterer, so that every scatterer has a range-dependent phase added to its phase history. When the phase history is reconstructed during processing to form the matched filter, this range-dependent term is still present. Thus, we must remove this phase term in order to focus the image properly.

This additional phase is introduced in the motion-compensation step because each echo is repositioned in range by a distance defined by the actual and reference orbit locations. In the motion-compensation step, the phase is advanced by an amount that corresponds to the distance of the scatterer at the location defined by the antenna boresight. Of course, for most of the range history, the scatterer is at a different distance from the antenna. Thus, the phase that is applied in motion compensation is only approximately correct over the phase history. Since we can calculate how much extra phase is added to the radar echoes at each position in the synthetic aperture, we remove that extra phase in this step by applying the second focus correction factor.

The magnitude of the phase correction depends on the amount of range migration for each scatterer at each point in time, and in the time-domain signal, echoes from many

scatterers at differing azimuth locations are present at each azimuth position. Thus, we cannot apply a single correction term to the time-domain signal. However, if we consider, instead, range migration as a function of frequency after applying a Fourier transform in the azimuth direction, we can apply a single correction to all scatterers at the same reference range simultaneously, which is analogous to the range migration resampling needed for range-Doppler processing. Since in the frequency domain we can represent the range migration as

$$r_{\text{migration}} = \frac{\lambda}{4\pi} \cdot \pi \cdot \frac{1}{f_{\text{rate}}} f^2 \quad (37)$$

we can apply the correction based on the idea that the range history is a function of the Doppler frequency. The required correction phase is the product of the migration distance and the gradient in the range of the motion-compensation phase

$$\begin{aligned}
 \phi_{\text{correction}} &= r_{\text{migration}} \cdot \frac{\partial}{\partial r} \left(\frac{4\pi}{\lambda} (r'(r) - r) \right) \Big|_{r=r_0} \\
 &= \frac{\lambda}{4 \cdot f_{\text{rate}}} \cdot f^2 \cdot \frac{\partial}{\partial r} \left(\frac{4\pi}{\lambda} (r'(r) - r) \right) \Big|_{r=r_0}. \quad (38)
 \end{aligned}$$

These two phase corrections suffice to focus the image properly.

VI. SUMMARY OF THE PROCESSING STEPS

In summary, our radar image generation steps include the following: Select a circular reference orbit, range compress each echo, apply motion compensation to move each echo to the reference track, Fourier transform the data in the azimuth direction, form the azimuth matched filter whose quadratic term reflects the motion-compensation baseline, remove the residual azimuth phase that results from the motion-compensation step, and inverse Fourier transform the data in azimuth. This produces the single-look complex data set that is needed for subsequent analysis.

VII. LIMITATIONS

Our approach for focusing the radar images will be less accurate under several different conditions, which must be assessed for each radar system configuration. These are the following.

- 1) If the motion-compensation baseline varies significantly over a single patch of raw data, the motion-compensation focus correction will not be correct everywhere. In our implementation, we assume that a single baseline is representative for the entire patch for the focus correction. While each echo is shifted in position for the instantaneous value of the baseline, focus correction is applied to the entire patch at once, which is a consequence of its frequency-domain implementation. If the variation in baseline is such that the chirp rate varies by more than about one part in the azimuth time-bandwidth product over the patch, some defocusing will occur.

- 2) If the baseline is not measured accurately enough, i.e., the trajectory is not known well enough, then the resulting interferogram will exhibit phase artifacts that are related to the error in position. For spaceborne sensors, which tend to be quite stable, this is not a significant problem unless the errors are very large. However, for airborne systems where there is a great deal of platform motion on short time scales, the phase artifacts will be quite visible and may mask the underlying desired phase signature.
- 3) Finally, if the orbit trajectory is such that there are very large velocities in the c or h direction, our estimates of the Doppler frequency will differ significantly for the actual and reference orbit cases. Processing the data at the incorrect Doppler centroid leads to defocusing and loss of signal. In our current implementation, we simply use the Doppler centroid as estimated from the raw data. Future implementations could include a refined Doppler estimation using the orbit data to avoid this problem.

Despite these known limitations, our method works quite well for existing spaceborne radar systems over the range of wavelengths and resolutions used in today's environmental radars.

VIII. INTERFEROGRAM FORMATION

The aforementioned steps lead to well-focused single-look complex SAR images with known coordinates for each point. The next step in most InSAR processors is the formation of the interferogram from a pair of these images. Interferogram formation is particularly simple if the coordinates of the two single-look images coincide, eliminating the difficult and time-consuming resampling step. Since we are free to choose any reference orbit for each image, selecting the same reference for both images of the InSAR pair leads directly to coincident images. Typically, we choose, as a reference, an orbit at the average height of the two scenes, with the average heading of the two scenes, and an along-track spacing set by the average velocity of the two scenes.

The processing equations as presented earlier locate the pixels, assuming that the planet surface is a perfect sphere with no topography. Thus, the images do not quite align perfectly, and offsets of up to a pixel are common. In addition, propagation delays through the ionosphere and troposphere are not yet accounted, leading to additional errors in pixel location. Thus, we apply a resampling based on image cross correlation to align the images optimally. However, because the misposition error is small, typically a pixel or two, this step is efficient, and the interferogram formation may be implemented without detailed topographic or propagation medium delay knowledge.

For more advanced processing methods, such as time series analysis, persistent scatterers [32], [33], [38]–[42], or small baseline analysis [34], [43], many images are required, rather than a single interferogram pair. In these cases, we still choose a single reference orbit based on the collection of scenes to be combined. Selection of an orbit that approximates an average of all of the orbits used is somewhat arbitrary but straightforward. For many applications, the exact reference orbit used is unimportant as long as the same orbit is used for all scenes.

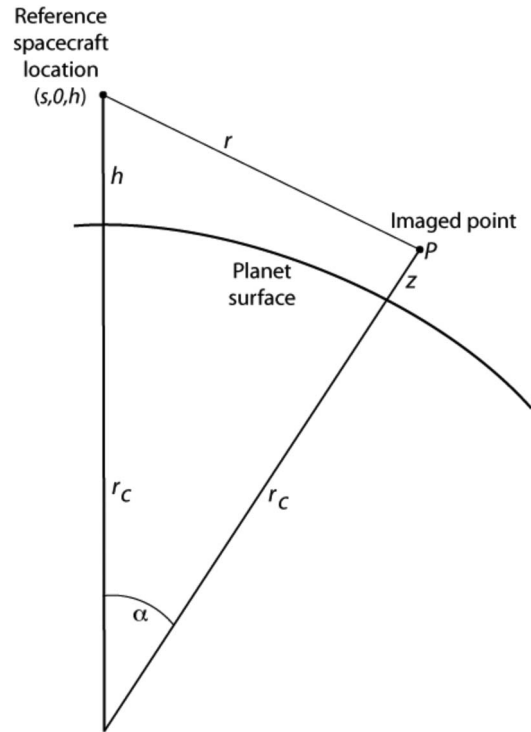


Fig. 6. Geometric construction for topographic correction. Imaged point P actually lies at an elevation z above the reference surface of a sphere of radius r_c . The Earth-centered angle α and the spacecraft height h are the same as defined in Fig. 1.

IX. TOPOGRAPHIC CORRECTION

The interferogram formed, as described in the previous section, does not contain the background phase pattern due to the general curvature of the Earth surface, since the motion-compensation method generates an effective InSAR baseline of zero for scatterers located on the surface. However, since the imaged area generally has topographic relief, the topographic phase contribution is still present. Therefore, for deformation applications, we must compensate for this phase term so that the “flattened” interferogram has only signals that are related to surface or propagation medium change.

Because the digital topographic data are often available for our study areas, we use the two-pass [1], [2] method for topographic phase compensation. In this method, we compute the latitude and longitude for each radar pixel, retrieve the elevation for that location from a digital elevation model (DEM), and compute and subtract the phase associated with a pixel at that elevation.

There is no closed-form solution to yield latitude, longitude, and elevation from range and azimuth radar coordinates, so we have developed an iterative approach that converges quickly to compute the elevation and location for each pixel. Consider the geometric construction of Fig. 6 in the following.

We initially let the scatterer height z be equal to zero, although another initial estimate will suffice as well. Given the reference orbit height, we can solve for the Earth-centered angle α as

$$\cos \alpha = \frac{(h + r_c)^2 + (r_c + z)^2 - \rho^2}{2(h + r_c)(r_c + z)}. \quad (39)$$

We next compute the sch coordinates of the pixel. The along-track coordinate s is related to the s coordinate of the satellite $s_{\text{satellite}}$ in the reference orbit coordinates by

$$s = s_{\text{satellite}} + r_c \tan^{-1} \left(\frac{f_d(r_c + h)\lambda r}{v(r_c^2 + (h + r_c)^2 - r^2)} \right) \quad (40)$$

where the second term on the right is the along-track distance for a pixel of the Doppler shift f_d . In our implementation, we compute the single-look complex images in a “skewed” geometry, so a range line of data corresponds to a constant squint direction so that only a single InSAR baseline vector is needed at each range line. This simplifies the bookkeeping requirements for topographic correction, but one could use deskewed images in which case the second term in (40) is not needed. The c and h coordinates follow from

$$c = -r_c \cos^{-1} \left(\frac{\cos \alpha}{\cos \beta} \right) \quad (41)$$

$$h = z \quad (42)$$

where β is the same as that defined in Fig. 1. Given an estimate of the pixel coordinates in the sch system, we convert the location to latitude/longitude/height coordinates. With this estimate of latitude and longitude, we then retrieve the elevation of the location from the DEM. This becomes our new estimate of z , and we repeat the process (39)–(42) to refine the estimate. We can iterate until the sequence converges, which typically takes two or three iterations. At the convergence of the iterative loop, we have the latitude, longitude, and elevation for each point in the image.

Finally, given the elevation of the pixel, we evaluate the phase expected from moving a scatterer from the reference sphere to its true elevation as

$$\phi_{\text{elevation}} = \frac{4\pi}{\lambda} \left(u_{\text{line-of-sight}}^{\text{elevation}} - u_{\text{line-of-sight}}^{\text{zero height}} \right) \bullet b(t) \quad (43)$$

where the u 's are the unit vectors to the pixel at elevation and on the reference sphere, respectively, and $b(t)$ is the InSAR baseline vector. Subtracting this phase from the interferogram at each point removes the topographic signature, leaving only the deformation and propagation variation phases.

Errors in orbit determination, plus unmodeled delays in the propagation medium, can lead to slight distortions in the topographically corrected interferograms. Thus, we further correct the images by registering them to the DEM transformed into radar coordinates. This registration corrects for additional pixel-scale shifts in the interferograms to yield a more geodetically precise result. Typical final registration shifts observed here are on the order of one pixel in the range direction and one to three pixels in the azimuth direction. The results for the sample ALOS data sets are tabulated in the following geodetic accuracy section (Table II).

X. GEOCODING

The final step that we apply in data processing is a resampling of the terrain-corrected interferogram onto an orthorectified grid. The interferogram before this stage is still sampled in

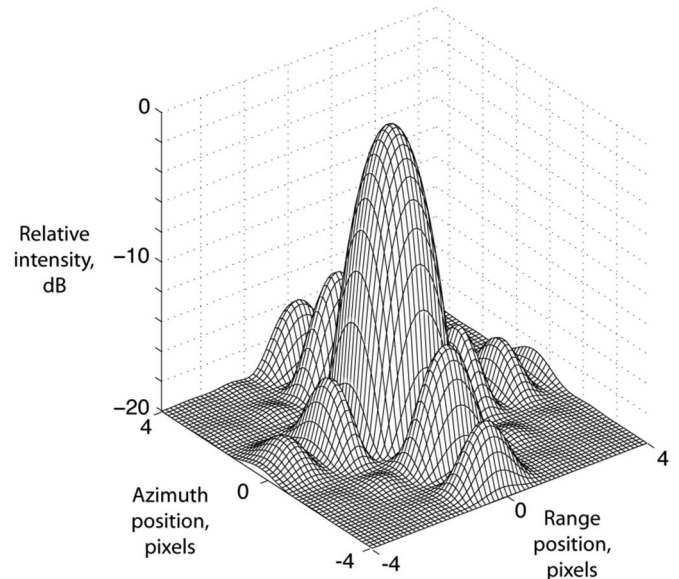


Fig. 7. Impulse response of the SAR processing module for the simulated ALOS data in a nominal geometry with an incidence angle of 34° . We computed the theoretical echoes for a point target corresponding to a 1500-m motion-compensation baseline and an InSAR baseline of about 3000 m. The half-power widths are 5.3 and 4.0 m in the slant range and in azimuth, respectively.

a uniform radar sensor coordinate system. It is essentially a range-Doppler coordinate system image where the along-track distance is expressed in meters rather than the Doppler frequency. The coordinates for each pixel are known in absolute position, as the transformation between the sch and absolute coordinates in an Earth-fixed rotating frame (which we refer to as the xyz coordinates) is well characterized once the topographic correction is applied. It is nonetheless more useful to resample the images to uniformly sampled latitude–longitude or Universal Transverse Mercator coordinates so that the data are more easily related to other data types. Our algorithms are not unusual; however, we are currently using a nearest neighbor interpolation during this step to avoid amplitude artifacts that follow from nonband-limited multilook interferogram data. This is an implementation choice, and if desired, the full single-look complex images may be resampled using the steps outlined earlier. We have chosen to work with multilook data to minimize disk and memory requirements.

XI. GEODETIC ACCURACY AND EXAMPLES

In this section, we present several images from our new processing system to illustrate its performance, especially as regards geodetic accuracy. Fig. 7 shows the impulse response of the SAR compression module for a simulated ALOS echo, where we have assumed an InSAR baseline of 3000 m, corresponding a motion-compensation baseline for each image of about 1500 m. The measured widths at half-power of the impulse response are roughly 5.3 m in the range dimension and 4.0 m in the azimuth dimension; theoretically, we would expect 5.35 m in the slant range and around 5 m (half the antenna length) in azimuth. The azimuth resolution is finer than we

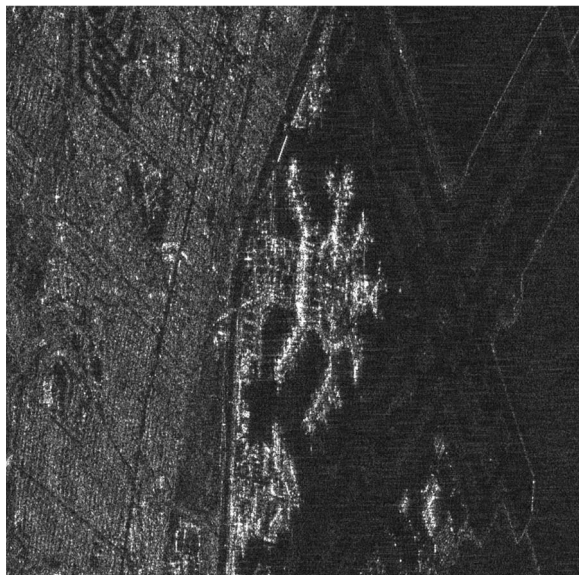


Fig. 8. Single-look complex image of the San Francisco airport as seen in the ALOS satellite data. The L-band wavelength leads to very dark runways at the right-hand side of the image, while the terminal structures stand out well. The slant range and azimuth pixel spacings of the image are 4.7 and 3.2 m, respectively. The image is well focused at this scale. Range (across) artifacts include sidelobes from the bright reflectors in the terminal area and interfering L-band signals that are visible over the darker parts of the image.

might expect as our simulator computes a phase history over a longer interval than the antenna illuminates.

In Fig. 8, we display a portion of a single-look complex image of the San Francisco airport from the ALOS satellite data acquired on February 28, 2008. The orbit and frame designators for this scene are 11162 and 740. The slant range (across) and azimuth (vertical) pixel spacings are 4.7 and 3.2 m, respectively. The resolution of the processed image is roughly one pixel, i.e., the image shows no appreciable blurring at this scale. Range sidelobes are visible from the strong reflectors on the airport terminal buildings. The horizontal artifacts that are visible mainly over the darker regions of the image are due to the L-band interference signals, which are many in the region. We have not filtered these interfering signals in this processing.

We assess the geodetic accuracy of our system in two ways: by processing an image containing known survey markers and by evaluating the shift in position between our images and reference data from existing DEMs. Three corner reflectors were installed in the Piñon Flat area in southern California by investigators at the Scripps Institution of Oceanography, University of California, San Diego, La Jolla [44]. One of these was aligned to return echoes in the direction of the ALOS satellite on its orbit track 213 in frame 660, which is an ascending orbit. We processed an interferogram on this track from orbits 7588 and 8259, acquired on June 28 and August 13, 2007. Two other reflectors were aligned with the descending orbit track, and we processed data from orbits 9360 and 10031, October 27 and December 12, 2007, track 534, and frame 2940. For all of these reflectors, we measured the inferred location from the interferograms and compared the results to a GPS ground survey done by scientists at Scripps. In Table I, we summarize our corner reflector location measurements from the

TABLE I
PIÑON FLAT CORNER REFLECTOR LOCATIONS

	Latitude	Longitude	Latitude	Longitude
Measurement	(deg)	(deg)	error (m)	error (m)
<u>Reflector aligned with ascending orbit</u>				
InSAR location, unregistered image	33.61233	-116.4570	9	-18
InSAR location, registered image	33.61215	-116.4567	-11	9
Ground GPS survey	33.61225	-116.4568	--	--
<u>Reflectors aligned with descending orbit</u>				
InSAR location, unregistered image	33.61215	-116.4579	-11	0
InSAR location, registered image	33.61213	-116.4577	-13	18
Ground GPS survey	33.61225	-116.4579	--	--
InSAR location, unregistered image	33.60729	-116.4517	-9	9
InSAR location, registered image	33.60727	-116.4516	-11	18
Ground GPS survey	33.60737	-116.4518	--	--

ALOS data and from the Scripps ground survey. The top line in each section of the table gives the observed location from our processor before alignment with a DEM, which is the “dead-reckoning” result. The middle line gives the location after a cross-correlation registration with a DEM, while the third line gives the location as determined from the ground geodetic survey. The disagreements here are on the order of 10–15 m, and the corner reflector is imaged with similar accuracy with and without registration to the DEM. Note that these results are quantized to the pixel spacing, though, because we use the nearest neighbor interpolation algorithm in this step of the implementation. We believe that this result is better than our typical accuracy across the entire image, however, as we discuss further in the following.

We present several processed interferogram data sets from ALOS measurements in Figs. 9–12. Fig. 9 shows an interferogram formed from the data acquired over southern California, centered over the town of Ventura. The image center latitude

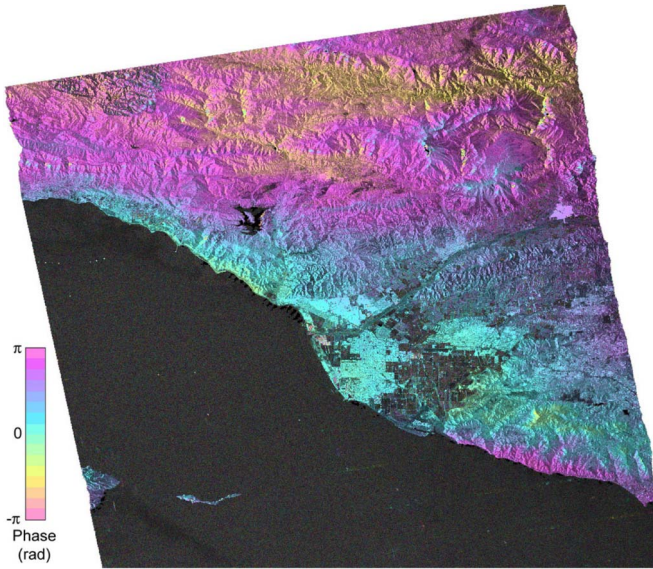


Fig. 9. ALOS interferogram of the Ventura area from the data acquired on June 22 and September 21, 2007. The phase signature is likely the variability of the atmosphere on the two days. The InSAR baseline is 100 m, and the illumination is from the left. The spacecraft motion is from south to north.

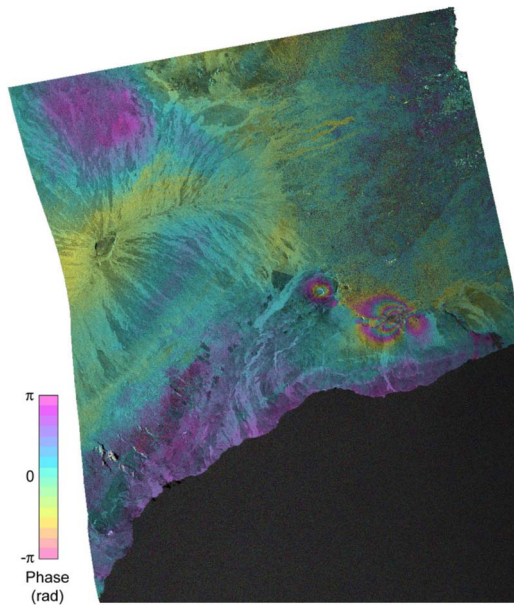


Fig. 10. ALOS interferogram from May 5 to June 20, 2007, over the Kilauea region of the island of Hawaii. An intrusion occurred in June 17–19 along the East Rift of the Kilauea Volcano $19^{\circ} 25' N$, $155^{\circ} 18' W$) and produced the clear crustal deformation phase signal. Additional phase variation, which is visible at the top portion and elsewhere on Mauna Loa, plus some signals along the coast, most likely results from atmospheric change. Illumination is from the left. The InSAR baseline is about 200 m.

and longitude are roughly $34^{\circ} N$, $119^{\circ} 15' W$, and the data were acquired on June 22, 2007 (orbit 7486 and frame 670) and September 21, 2007 (orbit 8828). In this interferogram, we see that there is a phase signature that is locally correlated with topography. However, globally, the phase does not depend on elevation, so we speculate that this is predominantly an atmospheric signature. The magnitude of the phase is comparable to previous reports of tropospheric phase in interferograms

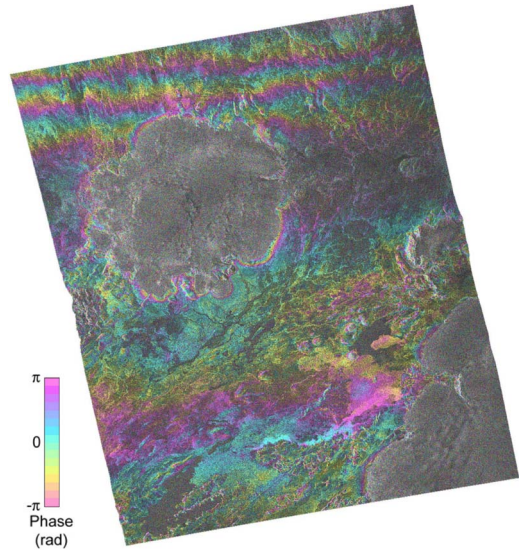


Fig. 11. ALOS interferogram of an area in Iceland, showing two glaciers and strong ionospheric artifacts. The change in the total electron content in the ionosphere is directly proportional to the phase delay and is visible as phase “bars.” The gradient in electron content is higher at the north than in the south. Data were acquired on September 2 and October 18, 2007, on orbits 8561 and 9232 (frame 1290). The InSAR baseline is about 300 m, and again, illumination is from the left.

[45]–[49]. The spacecraft moves from south to north, and the illumination is from the left.

In Fig. 10, we present an ALOS interferogram from orbits 6802 and 7473 (May 5 and June 20, 2007) over the Kilauea region of the island of Hawaii. Illumination again is from the left. In this image, there is a clear crustal deformation signal from an intrusion in June 17–19 along the East Rift of the Kilauea Volcano. The intrusion along the rift is accompanied by a deflation at the Kilauea Caldera. Additional phase signals, such as at the topmost portion of Mauna Loa and elsewhere on this volcano, plus some signals along the coast, most likely result from atmospheric change.

A different sort of artifact is visible in Fig. 11, which is an ALOS interferogram of glaciated terrain in Iceland (image center is approximately $64^{\circ} 40' N$, $18^{\circ} 30' W$). The illumination is again from the left. This image shows the phase “bars” that are aligned roughly with the range direction, mainly in the top part of the image, but are also visible in the southern third of the image. The northern artifacts are narrower than those in the south. We speculate that these phase patterns are due to the variations in the ionosphere rather than the troposphere, because they are also associated with the azimuth pixel shifts that would result from the gradients in the ionospheric electron content. The pixel shifts are most easily seen in the correlation image (see Fig. 12), where they cause similar bars of decorrelation as the two single look complex images do not align well. Tropospheric phase patterns would not be significant here because the surface temperature is low, so that the partial pressure of water vapor, which is responsible for most of the variable atmospheric signal [48], is very low. The interferogram decorrelates significantly over the glaciers near the image center and the southeast corner of the image, likely due to surface melt or motion.

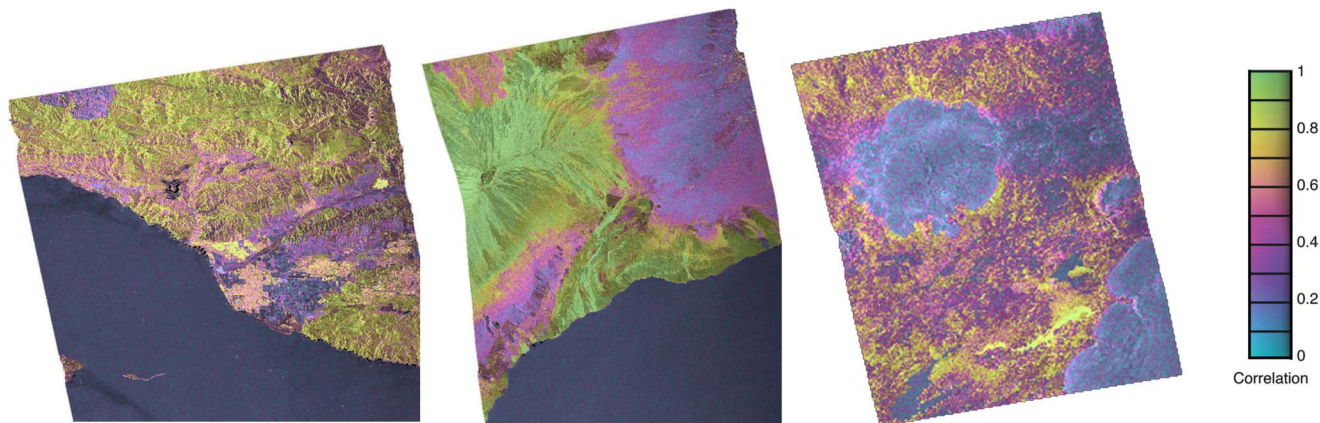


Fig. 12. Correlation images for the three scenes shown in Figs. 9–11. The Ventura image is at the left, Hawaii is at the center, and Iceland is at the right. Correlations range from near unity to essentially uncorrelated; hence, they are a representative of surface effects. The decorrelation band running across the Iceland image over the upper glacier is probably from pixel misposition due to electron density gradients in the ionosphere.

TABLE II
IMAGE REGISTRATION OFFSETS

Scene	Range offset	Azimuth offset	Additional stretch	
	at center (m)	at center (m)	Range (m)	Azimuth (m)
Ventura	-15.8	18.2	9.4	15.2
Hawaii	-21.5	24.0	14.1	25.4
Iceland	2.0	2.9	44.0	29.4

The correlation images for all three scenes of Figs. 9–11 are shown in Fig. 12. The correlations are generally high, except over water and over the glaciers in the Iceland image. The correlation drops over the vegetated area in the Hawaii image due to surface change as the vegetation changes over time. The Iceland image, in addition, shows a significant band of decorrelation near the northern glacier where there is the greatest shift in azimuth position due to electron content gradients in the ionosphere.

We can further characterize the geodetic accuracy of the processing system by examining the image registration shift needed to align the processed interferograms with the DEM that is used to correct the interferogram for elevation. In Table II, we list the offsets in range and azimuth (in meters), which are required to align the image with the DEM. We also list in the right-hand columns the additional amount of stretch that is required to align the remainder of the points with the DEM. This extra stretch tends to be great at the image corners. We can see that the image-center offset ranges from -22 to 24 m, and the additional image distortion that is needed to align with a reference DEM can be up to 44 m at one corner of the Iceland image.

XII. CONCLUSION

Modern satellite orbit determination produces trajectories that are extremely accurate. A precise knowledge of the satellite position enables processing of the InSAR images that are

accurate in position at the 10 -m level and are focused to the pixel level without requiring autofocus procedures. We have developed a processing approach that capitalizes on accurate orbit information to implement an efficient and robust InSAR processing package of software.

We have used the motion-compensation algorithms to propagate the raw radar echoes from their initial locations to a reference orbit that is chosen to simplify the pixel location and to focus equations, so that the implementation is both accurate and efficient. By choosing a single reference orbit for a collection of radar passes, pairs of scenes for interferogram formation or stacks of scenes as needed for persistent scattering or small baseline subset analysis are all produced in the same coordinate system so that the coregistration of the scenes is very easy, and it does not require the detailed image matching that haunts many InSAR processing runs. Motion compensation introduces two phase terms in the scatterer phase histories, which require correction in the processor, but these are easily applied using frequency-domain methods. The resulting single-look complex radar images are very well focused using only the orbit information for the radar satellite.

We have processed several radar images from the data acquired by the ALOS PALSAR instrument and L-band radar satellite. We have first assessed the geodetic accuracy by comparing the observed locations of a set of radar corner reflectors located in the Piñon Flat area in California. Corner reflector positions were accurate at the 10 – 20 -m level in our images. We have also processed interferograms from California, Hawaii, and Iceland and calculated the image location error by coregistering the images with DEMs. These images also showed 10 -m errors in position. We have also found out that the images had to be stretched up to 40 m so that all points in the radar scene matched the locations in the elevation model data. We speculate that these offsets are mainly due to unmodeled ionospheric and tropospheric effects or other unknown instrumental errors. Nonetheless, the data products are sufficiently accurate for many geophysical surface studies.

The overall set of processing equations may be implemented efficiently on modern multicore desktop computers so that, combined with the robustness of the approach, a reliable desktop generation of interferograms on cheap hardware is realized.

REFERENCES

- [1] D. Massonnet, M. Rossi, C. Carmona, F. Adragna, G. Peltzer, K. Feigl, and T. Rabaute, "The displacement field of the Landers earthquake mapped by radar interferometry," *Nature*, vol. 364, no. 6433, pp. 138–142, Jul. 1993.
- [2] H. A. Zebker, P. A. Rosen, R. M. Goldstein, A. Gabriel, and C. Werner, "On the derivation of coseismic displacement fields using differential radar interferometry: The Landers earthquake," *J. Geophys. Res.—Solid Earth*, vol. 99, no. B10, pp. 19 617–19 634, Oct. 10, 1994.
- [3] G. Peltzer, P. Rosen, F. Rogez, and K. Hudnut, "Postseismic rebound in fault step-overs caused by pore fluid flow," *Science*, vol. 273, no. 5279, pp. 1202–1204, Aug. 30, 1996.
- [4] W. Thatcher and D. Massonnet, "Crustal deformation at Long Valley Caldera, eastern California, 1992–1996 inferred from satellite radar interferometry," *Geophys. Res. Lett.*, vol. 24, no. 20, pp. 2519–2522, 1997.
- [5] C. Wicks, W. Thatcher, and D. Dzurisin, "Migration of fluids beneath Yellowstone Caldera inferred from satellite radar interferometry," *Science*, vol. 282, no. 5388, pp. 458–462, Oct. 1998.
- [6] F. Amelung, S. Jonsson, H. A. Zebker, and P. Segall, "Widespread uplift and trapdoor faulting on Galapagos volcanoes observed with radar interferometry," *Nature*, vol. 407, no. 6807, pp. 993–996, Oct. 26, 2000.
- [7] S. Jonsson, H. Zebker, P. Segall, and F. Amelung, "Fault slip distribution of the 1999 Mw 7.1 Hector Mine, California, earthquake, estimated from satellite radar and GPS measurements," *Bull. Seismol. Soc. Amer.*, vol. 92, no. 4, pp. 1377–1389, May 2002.
- [8] M. Pritchard and M. Simons, "A satellite geodetic survey of large-scale deformation of volcanic centers in the central Andes," *Nature*, vol. 418, no. 6894, pp. 167–171, Jul. 2002.
- [9] R. M. Goldstein, H. Engelhardt, B. Kamb, and R. M. Frolich, "Satellite radar interferometry for monitoring ice sheet motion: Application to an Arctic ice stream," *Science*, vol. 262, no. 5139, pp. 1525–1530, Dec. 3, 1993.
- [10] E. Rignot, K. C. Jezek, and H. G. Sohn, "Ice flow dynamics of the Greenland ice sheet from SAR interferometry," *Geophys. Res. Lett.*, vol. 22, no. 5, pp. 575–578, 1995.
- [11] I. R. Joughin, R. Kwok, and M. A. Fahnestock, "Interferometric estimation of three-dimensional ice-flow using ascending and descending passes," *IEEE Trans. Geosci. Remote Sens.*, vol. 36, no. 1, pp. 25–37, Jan. 1998.
- [12] E. Rignot, "Fast recession of an Antarctic Glacier," *Science*, vol. 281, no. 5376, pp. 549–551, Jul. 1998.
- [13] R. R. Forster, E. Rignot, B. L. Isacks, and K. Jezek, "Interferometric radar observations of Glaciars Europa and Penguin, Hielo Patagonico Sur, Chile," *J. Glaciol.*, vol. 45, no. 150, pp. 325–337, 1999.
- [14] E. Hoen and H. A. Zebker, "Penetration depths inferred from interferometric volume decorrelation observed over the Greenland ice sheet," *IEEE Trans. Geosci. Remote Sens.*, vol. 38, no. 6, pp. 2571–2583, Nov. 2000.
- [15] D. L. Galloway, K. W. Hudnut, S. E. Ingebritsen, S. R. Phillips, G. Peltzer, F. Rogez, and P. A. Rosen, "Detection of aquifer system compaction and land subsidence using interferometric synthetic aperture radar, Antelope Valley, Mojave Desert, California," *Water Resour. Res.*, vol. 34, no. 10, pp. 2573–2585, 1998.
- [16] D. E. Alsdorf, J. M. Melack, T. Dunne, A. K. Mertes, L. L. Hess, and L. C. Smith, "Interferometric measurements of water level changes on the Amazon flood plain," *Nature*, vol. 404, no. 6774, pp. 174–177, Mar. 2000.
- [17] J. Hoffmann, H. A. Zebker, D. L. Galloway, and F. Amelung, "Seasonal subsidence and rebound in Las Vegas Valley, Nevada, observed by synthetic aperture radar interferometry," *Water Resour. Res.*, vol. 37, no. 6, pp. 1551–1566, 2001.
- [18] R. N. Treuhaft and P. R. Siqueira, "Vertical structure of vegetated land surfaces from interferometric and polarimetric radar," *Radio Sci.*, vol. 35, no. 1, pp. 141–177, 2000.
- [19] K. Papathanassiou and S. R. Cloude, "Single-baseline polarimetric SAR interferometry," *IEEE Trans. Geosci. Remote Sens.*, vol. 39, no. 11, pp. 2352–2363, Nov. 2001.
- [20] J. Askne, M. Santoro, G. Smith, and J. E. S. Fransson, "Multitemporal repeat-pass SAR interferometry of boreal forests," *IEEE Trans. Geosci. Remote Sens.*, vol. 41, no. 7, pp. 1540–1550, Jul. 2003.
- [21] H. A. Zebker and R. M. Goldstein, "Topographic mapping from interferometric synthetic aperture radar observations," *J. Geophys. Res.*, vol. 91, no. B5, pp. 4993–4999, 1986.
- [22] J. O. Hagberg and L. M. H. Ulander, "On the optimization of interferometric SAR for topographic mapping," *IEEE Trans. Geosci. Remote Sens.*, vol. 31, no. 1, pp. 303–306, Jan. 1993.
- [23] J. Moreira, M. Schwabisch, G. Fornaro, R. Lanari, R. Bamler, D. Just, U. Steinbrecher, H. Breit, M. Eineder, G. Granceschetti, D. Geudtner, and H. Rinkel, "X-SAR interferometry: First results," *IEEE Trans. Geosci. Remote Sens.*, vol. 33, no. 4, pp. 950–956, Jul. 1995.
- [24] T. G. Farr, P. A. Rosen, E. Caro, R. Crippen, R. Duren, S. Hensley, M. Kobrick, M. Paller, E. Rodriguez, L. Roth, D. Seal, S. Shaffer, J. Shimada, J. Umland, M. Werner, M. Oskin, D. Burbank, and D. Alsdorf, "The Shuttle Radar Topography Mission," *Rev. Geophys.*, vol. 45, no. 2, p. RG2004, 2007.
- [25] B. D. Tapley, J. C. Ries, G. W. Davis, R. J. Eanes, B. E. Schultz, C. K. Shum, M. M. Watkins, J. Marshall, A. Nerem, and R. S. Putney, "Precision orbit determination for TOPEX/POSEIDON," *J. Geophys. Res.*, vol. 99, no. C12, pp. 24 383–24 404, Dec. 1994.
- [26] R. Scharroo and P. Visser, "Precise orbit determination and gravity field improvement for the ERS satellites," *J. Geophys. Res.*, vol. 103, no. C4, pp. 8113–8128, 1998.
- [27] P. H. Andersen, K. Aksnes, and H. Skonjord, "Precise ERS-2 orbit determination using SLR, PRARE, and RA observations," *J. Geodesy*, vol. 72, no. 7/8, pp. 421–429, 1998.
- [28] S. Katagiri and Y. Yamamoto, "Technology of precise orbit determination," *Fujitsu Sci. Tech. J.*, vol. 44, no. 4, pp. 401–409, Oct. 2008.
- [29] J. J. Mohr and S. N. Madsen, "Geometric calibration of ERS satellite SAR images," *IEEE Trans. Geosci. Remote Sens.*, vol. 39, no. 4, pp. 842–850, Apr. 2001.
- [30] D. T. Sandwell, D. Myer, R. Mellors, M. Shimada, B. Brooks, and J. Foster, "Accuracy and resolution of ALOS interferometry: Vector deformation maps of the Father's Day Intrusion at Kilauea," *IEEE Trans. Geosci. Remote Sens.*, vol. 46, pt. 1, no. 11, pp. 3524–3534, Nov. 2008.
- [31] D. T. Sandwell and L. Sichoix, "Topographic phase recovery from stacked ERS interferometry and a low resolution digital elevation model," *J. Geophys. Res.*, vol. 105, no. B12, pp. 28 211–28 222, Dec. 2000.
- [32] A. Ferretti, C. Prati, and F. Rocca, "Permanent scatterers in SAR interferometry," *IEEE Trans. Geosci. Remote Sens.*, vol. 39, no. 1, pp. 8–20, Jan. 2001.
- [33] A. Ferretti, C. Prati, and F. Rocca, "Nonlinear subsidence rate estimation using permanent scatterers in differential SAR interferometry," *IEEE Trans. Geosci. Remote Sens.*, vol. 38, pt. 1, no. 5, pp. 2202–2212, Sep. 2000.
- [34] P. Berardino, G. Fornaro, R. Lanari, and E. Sansosti, "A new algorithm for surface deformation monitoring based on small baseline differential SAR interferograms," *IEEE Trans. Geosci. Remote Sens.*, vol. 40, no. 11, pp. 2375–2383, Nov. 2002.
- [35] J. C. Curlander and R. N. McDonough, *Synthetic Aperture Radar*. New York: Wiley-Interscience, 1991.
- [36] S. M. Buckley, "Radar interferometry measurement of land subsidence," Ph.D. Dissertation, Univ. Texas, Austin, TX, 2000.
- [37] C. V. Jakowatz, D. E. Wahl, P. H. Eichel, D. C. Ghiglia, and P. A. Thompson, *Synthetic Aperture Radar: A Processing Approach*. Boston, MA: Kluwer, 1996.
- [38] A. Hooper, P. Segall, and H. Zebker, "Persistent scatterer interferometric synthetic aperture radar for crustal deformation analysis, with application to Volcan Alcedo, Galapagos," *J. Geophys. Res.*, vol. 112, no. B7, p. B07407, 2007.
- [39] S. Lyons and D. Sandwell, "Fault creep along the southern San Andreas from interferometric synthetic aperture radar, permanent scatterers, and stacking," *J. Geophys. Res.*, vol. 108, no. B1, p. 2047, 2003.
- [40] C. Colesanti, A. Ferretti, C. Prati, and F. Rocca, "Monitoring landslides and tectonic motions with the permanent scatterers technique," *Eng. Geol.*, vol. 68, no. 1/2, pp. 3–14, Feb. 2003.
- [41] G. E. Hilley, R. Bürgmann, A. Ferretti, F. Novali, and F. Rocca, "Dynamics of slow-moving landslides from permanent scatterer analysis," *Science*, vol. 304, no. 5679, pp. 1952–1955, Jun. 2004.
- [42] P. Shanker and H. Zebker, "Persistent scatterer selection using maximum likelihood estimation," *Geophys. Res. Lett.*, vol. 34, no. 22, p. L22301, 2007.
- [43] R. Lanari, F. Casu, M. Manzo, G. Zeni, P. Berardino, M. Manuta, and A. Pepe, "An overview of the small baseline subset algorithm: A DInSAR technique for surface deformation analysis," *Pure Appl. Geophys.*, vol. 164, no. 4, pp. 637–661, Apr. 2007.
- [44] D. Sandwell, personal communication.
- [45] H. A. Zebker, P. A. Rosen, and S. Hensley, "Atmospheric effects in interferometric synthetic aperture radar surface deformation and topographic maps," *J. Geophys. Res.*, vol. 102, no. B4, pp. 7547–7563, 1997.
- [46] R. F. Hanssen, T. M. Weckwerth, H. A. Zebker, and R. Klees, "High-resolution water vapor mapping from interferometric radar measurements," *Science*, vol. 283, no. 5406, pp. 1297–1299, Feb. 1999.
- [47] R. Hanssen, *Radar Interferometry: Data Interpretation and Error Analysis*. Dordrecht, Netherlands: Kluwer, 2001.

- [48] F. Onn and H. A. Zebker, "Correction for interferometric synthetic aperture radar atmospheric phase artifacts using time series of zenith wet delay observations from a GPS network," *J. Geophys. Res.*, vol. 111, no. B9, p. B09102, Sep. 23, 2006.
- [49] J. Foster, B. Brooks, T. Cherubini, C. Shacat, S. Businger, and C. L. Werner, "Mitigating atmospheric noise for InSAR using a high resolution weather model," *Geophys. Res. Lett.*, vol. 33, no. 16, p. L16304, 2006.



Howard A. Zebker (M'87–SM'89–F'99) received the B.S. degree from the California Institute of Technology, Pasadena, in 1976, the M.S. degree from the University of California, Los Angeles, in 1979, and the Ph.D. degree from Stanford University, Stanford, CA, in 1984.

He is currently a Professor of geophysics and electrical engineering with Stanford University, where his research group specializes in radar remote sensing, especially InSAR, of the Earth and planets. He has more than 30 years of experience in spaceborne radar, beginning with the SEASAT program in the 1970s and currently with the radar science team on the Cassini mission of the National Aeronautics and Space Administration (NASA). Other satellite programs where he has contributed include NASA's Spaceborne Imaging Radar-A, B, and C; the Magellan Mission to Venus; and the Voyager Mission to the outer planets. His major research focus is on the development of radar as a technique and the application of this technique to basic Earth science. He has published over 300 scholarly articles on remote sensing, and he teaches several courses on remote sensing at Stanford University to undergraduate and graduate students alike.

Dr. Zebker is a Fellow of the Electromagnetics Academy and a member of the American Geophysical Union.

Scott Hensley received the B.S. degrees in mathematics and physics from the University of California, Irvine, and the Ph.D. degree in mathematics from the State University of New York, Stony Brook, where he specialized in the study of differential geometry.

Subsequent to graduating, he was with Hughes Aircraft Company on a variety of radar systems, including the Magellan radar. Since 1992, he has been with the Jet Propulsion Laboratory, California Institute of Technology, Pasadena, CA, where he studies advanced radar techniques for geophysical applications. His research has involved using both the stereo and interferometric data acquired by the Magellan spacecraft at Venus and using the European Remote Sensing Satellite-1, Japanese Earth Resources Satellite-1, and Spaceborne Imaging Radar-C data for differential interferometry studies of earthquakes and volcanoes. His current research also includes studying the amount of penetration into the vegetation canopy using simultaneous L- and C-band topographic synthetic aperture radar measurements and repeat-pass airborne interferometry data collected at lower frequencies (P-band). He was the Technical Lead of the Shuttle Radar Topography Mission Interferometric Processor Development Team for a shuttle-based interferometric radar that is used to map the Earth's topography in the $\pm 60^\circ$ latitude. He is currently the Principal Investigator of the Uninhabited Aerial Vehicle Synthetic Aperture Radar program that is developing a repeat-pass radar interferometry capability for use on conventional or unmanned aerial vehicles. Recently, he began working with the Goldstone Solar System Radar to generate topographic maps of the lunar surface.

Piyush Shanker, photograph and biography not available at the time of publication.



Cody Wortham received the B.S. and M.S. degrees in electrical engineering from the Georgia Institute of Technology, Atlanta, in 2005 and 2007, where he focused on space-time signal processing for radar interference cancellation. Since 2007, he has been working toward the Ph.D. degree in electrical engineering at Stanford University, Stanford, CA.

His research interests include InSAR processing and vector time-series from multiple InSAR geometries.